J. Fluid Mech. (2023), *vol*. 977, A50, doi:10.1017/jfm.2023.1016

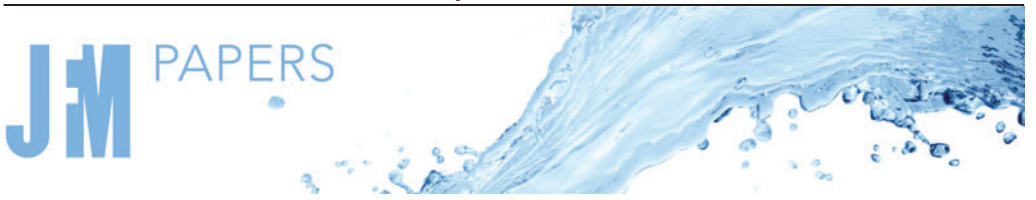

Capillary-lubrication force exerted on a two-dimensional particle moving towards a thin fluid film

Aditya Jha[1], **Yacine Amarouchene**[1] **and Thomas Salez**[1,†]

[1]Univ. Bordeaux, CNRS, LOMA, UMR 5798, F-33400 Talence, France

(Received 21 June 2023; revised 21 November 2023; accepted 25 November 2023)

A rigid object moving in a viscous fluid and in close proximity to an elastic wall experiences self-generated elastohydrodynamic interactions. This has been the subject of intense research activity, with recent and growing attention given to the particular case of elastomeric and gel-like substrates. Here, we address the situation where the elastic wall is replaced by a capillary surface. Specifically, we analyse the lubrication flow generated by the prescribed normal motion of a rigid infinite cylinder near the deformable interface separating two immiscible and incompressible viscous fluids. Using a combination of analytical and numerical treatments, we compute the emergent capillary-lubrication force at leading order in capillary compliance, and characterize its dependencies with the interfacial tension, viscosities of the fluids, and length scales of the problem. Interestingly, we identify two main contributions: (i) a velocity-dependent adhesive-like force; (ii) an acceleration-dependant inertia-like force. Our results may have implications for the mobility of colloids near complex interfaces and for the motility of confined microbiological entities.

Key words: capillary flows, thin films, lubrication theory

1. Introduction

The motion of a rigid object in a fluid has been well studied during the last couple of centuries (Batchelor 1967). In a bulk situation, for an incompressible Newtonian viscous fluid, the hydrodynamic force exerted on the object depends on its shape, size and speed, as well as on the fluid viscosity and frictional boundary conditions. Adding a neighbouring rigid wall to the latter problem was an obvious extension to consider, in view of the

† Email address for correspondence: thomas.salez@cnrs.fr

historical importance of lubricated contact mechanics in industry, but also because of the modern trends in miniaturization, colloidal surface science and confined biological physics. Such a modification introduces a symmetry breaking as well as different flow boundary conditions (Goldman, Cox & Brenner 1967; O'Neill & Stewartson 1967; Cooley & O'Neill 1969; Jeffrey & Onishi 1981). A classical result from these studies shows that the force felt by a spherical particle approaching a no-slip wall increases inversely with the gap thickness, which implies no contact in finite time. Hocking (1973) also explored the effect of slippage at the solid boundary, leading to a logarithmic factor and a contact in finite time. Happel & Brenner (1983) provided a detailed account of this situation, including the related case of suspensions.

In view of the growing interest in soft matter towards complex materials, such as elastomers, gels or biological membranes, replacing the above rigid wall by an elastic boundary became of central importance. In such a context, the influence of the elastic response on the lubrication flow and associated forces and torques was addressed in both the normal (Balmforth, Cawthorn & Craster 2010; Leroy & Charlaix 2011; Leroy *et al.* 2012; Villey *et al.* 2013; Wang, Dhong & Frechette 2015; Karan, Chakraborty & Chakraborty 2018, 2020, 2021) and transverse (Sekimoto & Leibler 1993; Beaucourt, Biben & Misbah 2004; Skotheim & Mahadevan 2005; Weekley, Waters & Jensen 2006; Urzay, Llewellyn Smith & Glover 2007; Snoeijer, Eggers & Venner 2013; Bouchet *et al.* 2015; Salez & Mahadevan 2015; Saintyves *et al.* 2016; Davies *et al.* 2018; Rallabandi *et al.* 2018; Vialar *et al.* 2019; Zhang *et al.* 2020; Essink *et al.* 2021; Bertin *et al.* 2022; Bureau, Coupier & Salez 2023) modes. This was achieved essentially by combining previous works on: (i) solid–solid contact and linear elasticity (Johnson 1985; Li & Chou 1997; Nogi & Kato 1997, 2002), and (ii) lubrication theory (Reynolds 1886; Oron, Davis & Bankoff 1997), resulting in the so-called soft-lubrication theory. These developments led in part to the design of non-invasive contactless mechanical probes for the rheology of soft, fragile and alive materials (Garcia *et al.* 2016; Basoli *et al.* 2018). Further studies then incorporated elements of complexity in the substrate's response, through e.g. viscoelasticity (Pandey *et al.* 2016; Guan *et al.* 2017; Kargar-Estahbanati & Rallabandi 2021; Zhang *et al.* 2022) and poroelasticity (Kopecz-Muller *et al.* 2023).

Interestingly, as materials get softer and increasingly liquid-like, solid capillarity takes the relay over bulk elasticity to eventually become the dominant restoring mechanism – a topic of recent and active research (Andreotti *et al.* 2016). As a consequence, investigating soft-lubrication-like couplings in situations where the flow-induced interfacial deformation is resisted mainly by surface tension appears to be a relevant task. In a series of seminal articles, Lee, Leal and colleagues calculated the forces felt by a sphere moving close to a fluid interface in Stokes flow (Lee, Chadwick & Leal 1979; Lee & Leal 1980, 1982; Berdan & Leal 1982; Geller, Lee & Leal 1986). Using Lorentz's reciprocal theorem, as well as a complete eigenfunction expansion in bipolar coordinates, they were able to exhibit the effects of the fluid interface – albeit in the regime where the gap between the sphere and the interface is large, and the interfacial deformation is negligible. It was found that the drag and torque acting on the sphere could be larger or smaller than their bulk counterparts, depending on the viscosities of the two layers. Related developments included the cases of slender objects (Yang & Leal 1983), bubbles and droplets (Vakarelski *et al.* 2010; Chan, Klaseboer & Manica 2011), living microorganisms (Trouilloud *et al.* 2008; Lopez & Lauga 2014), slippery interfaces (Rinehart *et al.* 2020) and air–water interfaces with surface-active contaminants (Maali *et al.* 2017; Bertin *et al.* 2021).

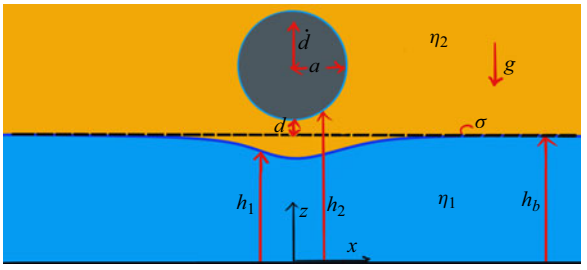

Figure 1. Schematic of the system. A rigid infinite cylinder moves with a prescribed velocity normal to a nearby capillary interface between two incompressible Newtonian viscous liquids. The ensemble is placed atop a rigid substrate. The origin of spatial coordinates is located at the interface between the rigid substrate and the bottom liquid layer ($z = 0$) under the centre of mass of the cylinder ($x = 0$).

While the above studies highlight clearly the richness and importance of motion near fluid interfaces, they focus on specific geometries and viscosity ratios. Hence the general capillary-lubrication regime has been scarcely explored so far. In the present paper, we thus investigate theoretically and numerically the lubrication flow and associated force generated by the prescribed normal motion of a rigid infinite cylinder near a deformable interface separating two immiscible and incompressible viscous fluids. We invoke a perturbative approach in dimensionless capillary compliance, and study the influence of the interfacial tension, viscosities of the fluids, and length scales of the problem on the resulting capillary-lubrication force.

The paper is organized as follows. We start by setting the general capillary-lubrication theoretical framework. Then the perturbation analysis is presented for the pressure and deformation fields up to first order in dimensionless capillary compliance, the latter being related directly to the capillary number. Finally, we discuss the results, compute quantitatively the capillary-lubrication force, and investigate the influence of all physical and geometrical parameters on the latter.

2. Capillary-lubrication theory

As shown in figure 1, we consider a rigid infinite cylinder of radius a moving in a fluid with a prescribed velocity normal to the nearby interface with a thin fluid film supported on a rigid substrate. The interface is characterized by its surface tension σ, and separates two incompressible Newtonian viscous liquids, with dynamic shear viscosities η_1 and η_2, as well as densities ρ_1 and $\rho_2 = \rho_1 - \delta\rho$ (with $\delta\rho > 0$). The acceleration due to gravity is denoted g. The thickness profile $h_1(x, t)$ of the bottom liquid layer depends on the horizontal position x as well as time t, and at large x, it equals the undeformed reference value h_b. The total thickness profile between the rigid substrate and the cylinder surface is denoted by $h_2(x, t)$. We also define the minimal distance $d(t) = h_2(0, t) - h_b$ between the undeformed fluid interface and the cylinder surface, the time derivative $\dot{d}(t)$ of which being the prescribed time-dependent velocity of the cylinder along z.

2.1. *Governing equations*

We neglect fluid inertia and assume the typical thicknesses, e.g. $h_1(0, t)$ and $h_2(0, t) - h_1(0, t)$, of the two relevant liquid films of the problem to be much smaller than the proper horizontal length scale – whether the latter is the cylinder radius a, the capillary length $\sqrt{\sigma/(g\delta\rho)}$, or the hydrodynamic radius $\sqrt{2ad}$ (Leroy & Charlaix 2011),

as discussed below. Therefore, we can invoke the lubrication theory (Reynolds 1886; Oron *et al.* 1997). Introducing the excess pressure fields $p_i(x, z, t)$ with respect to the hydrostatic contributions, and the horizontal velocity fields $u_i(x, z, t)$, in the two liquids indexed by $i = 1, 2$, the incompressible Stokes equations thus read, within the classical lubrication limit,

$$\frac{\partial p_i}{\partial z} = 0, \tag{2.1}$$

$$\frac{\partial p_i}{\partial x} = \eta_i \frac{\partial^2 u_i}{\partial z^2}. \tag{2.2}$$

Also, since typically the dominant flow is located only in the lubricated-contact region underneath the cylinder, we approximate the shape of the cylindrical surface by its parabolic expansion, leading to

$$h_2(x, t) \simeq h_b + d(t) + \frac{x^2}{2a}. \tag{2.3}$$

Finally, we close the set of equations by setting the flow boundary conditions. We impose no-slip at the three interfaces, as well as tangential and normal stress balances at the fluid interface. Hence at $z = 0$ one has

$$u_1 = 0, \tag{2.4}$$

while at $z = h_1$ one has (Leal 2007)

$$u_2 = u_1, \tag{2.5}$$

$$\eta_2 \frac{\partial u_2}{\partial z} = \eta_1 \frac{\partial u_1}{\partial z}, \tag{2.6}$$

$$p_2 - p_1 \simeq \sigma \frac{\partial^2 h_1}{\partial x^2} + g(h_b - h_1)\,\delta\rho \tag{2.7}$$

(where the latter equation is valid under the small-slope approximation), and at $z = h_2$ one has

$$u_2 = 0. \tag{2.8}$$

Let us now non-dimensionalize the equations through

$$\left.\begin{gathered} h_1(x, t) = d^* H_1(X, T), \quad h_2(x, t) = d^* H_2(X, T), \quad x = lX, \\ z = d^* Z, \quad t = \frac{d^*}{c} T, \quad d(t) = d^* D(T), \\ u_1(x, z, t) = \frac{lc}{d^*} U_1(X, Z, T), \quad u_2(x, z, t) = \frac{lc}{d^*} U_2(X, Z, T), \\ p_1(x, t) = \frac{\eta_2 c l^2}{d^{*3}} P_1(X, T), \\ p_2(x, t) = \frac{\eta_2 c l^2}{d^{*3}} P_2(X, T), \quad h_b = d^* H_b, \quad \dot{d}(t) = c\,\dot{D}(T), \end{gathered}\right\} \tag{2.9}$$

with the hydrodynamic radius $l = \sqrt{2ad^*}$, and where d^* and c represent some characteristic vertical length and vertical velocity scales that can be set to e.g. $d(0)$ and

$\dot{d}(0)$, respectively. Moreover, the viscosity ratio is denoted by $M = \eta_1/\eta_2$ and controls the effective slip length at the interface through (2.6). Specifically, an effective rigid-like no-slip condition (i.e. $u_2 = 0$) is obtained for $M \to \infty$, while an effective full-slip condition (i.e. infinite slip length) is obtained for $M \to 0$. Using these dimensionless variables, (2.3) becomes

$$H_2(X, T) = H_b + D(T) + X^2. \tag{2.10}$$

Solving (2.1) and (2.2) together with the boundary conditions (2.4)–(2.6) and (2.8) gives the velocity profiles

$$\begin{aligned} U_1 = {} & -P_2' \frac{(H_2 - H_1)^2 Z}{2[H_1 + M(H_2 - H_1)]} \\ & + P_1' \left\{ \frac{Z^2}{2M} + \frac{Z}{H_1 + M(H_2 - H_1)} \left[H_1(H_1 - H_2) - \frac{H_1^2}{2M} \right] \right\}, \end{aligned} \tag{2.11}$$

$$\begin{aligned} U_2 = {} & P_2' \left[\frac{Z^2 - H_2^2}{2} - (Z - H_2) \left\{ H_1 + \frac{M(H_2 - H_1)^2}{2[H_1 + M(H_2 - H_1)]} \right\} \right] \\ & + P_1' \frac{(Z - H_2) H_1^2}{2[H_1 + M(H_2 - H_1)]}, \end{aligned} \tag{2.12}$$

where the prime symbol corresponds to the partial derivative with respect to X. We then calculate the flow rates within the two liquid films as

$$Q_1 = \int_0^{H_1} U_1 \, \mathrm{d}Z = -P_2' \frac{H_1^2 (H_1 - H_2)^2}{4[H_1 + M(H_2 - H_1)]} - P_1' \frac{H_1^3 [H_1 + 4M(H_2 - H_1)]}{12M[H_1 + M(H_2 - H_1)]}, \tag{2.13}$$

$$Q_2 = \int_{H_1}^{H_2} U_2 \, \mathrm{d}Z = -P_2' \frac{(H_2 - H_1)^3}{12} \frac{4H_1 + M(H_2 - H_1)}{H_1 + M(H_2 - H_1)} - P_1' \frac{H_1^2 (H_2 - H_1)^2}{4[H_1 + M(H_2 - H_1)]}. \tag{2.14}$$

Thanks to volume conservation, the flow rates allow us to write down the two thin-film equations, which read

$$\frac{\partial H_1}{\partial T} + Q_1' = 0, \tag{2.15}$$

$$\frac{\partial (H_2 - H_1)}{\partial T} + Q_2' = 0. \tag{2.16}$$

Finally, (2.7) reads, in dimensionless form,

$$H_1'' + Bo\,(H_b - H_1) = \kappa (P_2 - P_1), \tag{2.17}$$

where $Bo = (l/l_c)^2$ denotes the Bond number of the problem, with $l_c = \sqrt{\sigma/(g\delta\rho)}$ the capillary length, and where $\kappa = Ca/\epsilon^4$ is the dimensionless capillary compliance of the fluid interface, with $Ca = \eta_2 c/\sigma$ a capillary number, and with $\epsilon = d^*/l$ and ϵH_b the two small lubrication parameters of the problem.

Altogether, since H_2 is known from (2.10) and the prescribed $D(T)$, there are actually three unknown fields in the problem: H_1, P_1 and P_2. These obey the set of three coupled

differential equations given by (2.15)–(2.17), together with the symmetry conditions at $X = 0$

$$P_i' = 0, \quad H_1' = 0, \tag{2.18a,b}$$

and the spatial boundary conditions at $X \to \infty$

$$P_i \to 0, \quad H_1 \to H_b. \tag{2.19a,b}$$

The whole study below is performed in terms of the dimensionless variables and dimensionless parameters provided above. We thus refer the reader to the present section for all the definitions.

3. Perturbation analysis

Following the approach of previous soft-lubrication studies (Sekimoto & Leibler 1993; Skotheim & Mahadevan 2005; Urzay *et al.* 2007; Salez & Mahadevan 2015; Pandey *et al.* 2016), we assume that $\kappa \ll 1$ and perform an expansion of the fields up to first order in κ, as

$$H_1 = H_b + \kappa\Delta + O(\kappa^2), \tag{3.1}$$

$$P_1 = P_{10} + \kappa P_{11} + O(\kappa^2), \tag{3.2}$$

$$P_2 = P_{20} + \kappa P_{21} + O(\kappa^2), \tag{3.3}$$

where $\kappa\Delta$ is the deformation profile of the fluid interface at first order in κ, and $\kappa^j P_{ij}$ is the excess pressure contribution of layer i at perturbation order j. We further impose the following symmetry and spatial boundary conditions (see (2.18*a*,*b*) and (2.19*a*,*b*)): $P_{ij}' = 0$ and $\Delta' = 0$ at $X = 0$, as well as $P_{ij} \to 0$ and $\Delta \to 0$ at $X \to \infty$.

3.1. *Zeroth-order solution*

At zeroth order in κ, the fluid interface is undeformed, and the bottom-film thickness profile is constant and equal to H_b. Equations (2.15) and (2.16) can then be solved analytically using the symmetry and boundary conditions on the pressure fields. This leads to

$$P_{10} = \frac{9M\dot{D}}{2H_b^2} \ln\left(1 + \frac{1}{\xi}\right), \tag{3.4}$$

$$P_{20} = \frac{9M^2\dot{D}}{2H_b^2}\left[\ln\left(1 + \frac{1}{\xi}\right) - \frac{1}{\xi} - \frac{1}{6\xi^2}\right], \tag{3.5}$$

where we have introduced the auxiliary variable $\xi(X, T) = M[D(T) + X^2]/H_b$. Interestingly, the zeroth-order excess pressure fields contain logarithmic terms, which differ notably from the rigid-substrate case where the excess pressure reads $P_s = -3\dot{D}/(D + X^2)^2$ (Jeffrey & Onishi 1981). Nevertheless, the logarithmic terms decay algebraically in the far field, as $\sim 1/X^2$, and the far-field expansion of the zeroth-order pressure field in the top layer reaches the solution for the no-slip rigid case, i.e. $P_{20} \simeq P_s$ at large X.

3.2. *First-order solution*

At first order in κ, (2.17) reads

$$\Delta'' - Bo\,\Delta = P_{20} - P_{10}. \tag{3.6}$$

The formal solution of (3.6), satisfying the above symmetry (see (2.18*a*,*b*)) and boundary (see (2.19*a*,*b*)) conditions, is

$$\Delta = \Delta_c \cosh(X\sqrt{Bo}) - \frac{1}{\sqrt{Bo}} \int_0^X \mathrm{d}y\,[P_{20}(y) - P_{10}(y)] \sinh[(y - X)\sqrt{Bo}], \tag{3.7}$$

where $\Delta_c = \Delta(X = 0, T) = (1/\sqrt{Bo}) \int_0^\infty \mathrm{d}y\,[P_{10}(y) - P_{20}(y)] \exp(-y\sqrt{Bo})$ is the central deformation of the fluid interface. This solution can be evaluated numerically for fixed parameters Bo, M and H_b, and a prescribed $D(T)$ trajectory.

In order to rationalize the asymptotic behaviours of the numerical solution, and to evaluate the central deformation, we employ an asymptotic-matching method, which is a usual approach for capillary problems (James 1974; Lo 1983; Dupré de Baubigny *et al.* 2015). To do so, we assume a scale separation between: (i) an inner problem characterized by the horizontal length scale l, where the dominant lubrication flow is located, and where gravity is absent; and (ii) an outer problem characterized by the capillary length l_c, where gravity regularizes the deformation. Specifically, we assume that $l \ll l_c$, i.e. $Bo \ll 1$. Let us first study the inner problem and associated inner solution $\Delta_{in}(X, T)$. In the inner region, where $X \ll 1/\sqrt{Bo}$, (3.6) can be approximated by

$$\Delta_{in}'' = P_{20} - P_{10}. \tag{3.8}$$

The solution of this equation, satisfying the symmetry condition $\Delta_{in}'(X = 0, T) = 0$, reads

$$\begin{aligned}\Delta_{in} = \mathcal{A} + \frac{9\dot{D}}{4H_b^2} \Bigg\{ & (M-1)MX^2 \ln\left[1 + \frac{H_b}{M(D+X^2)}\right] \\ & + (1-M)(H_b + MD)\ln[H_b + M(D+X^2)] + [H_b + (M-1)D]M\ln(D+X^2) \\ & + 4\sqrt{D}\,M(1-M)X\tan^{-1}\left(\frac{X}{\sqrt{D}}\right) + 4M(M-1)X\sqrt{D + \frac{H_b}{M}}\tan^{-1}\left(\frac{X}{\sqrt{D + \frac{H_b}{M}}}\right) \\ & - \frac{2MH_bX}{\sqrt{D}}\tan^{-1}\left(\frac{X}{\sqrt{D}}\right) - \frac{H_b^2}{6D^{3/2}}X\tan^{-1}\left(\frac{X}{\sqrt{D}}\right)\Bigg\}, \end{aligned} \tag{3.9}$$

where $\mathcal{A}$ is a function of T only. The far-field behaviour of this inner solution reads

$$\begin{aligned}\Delta_{in} \sim \mathcal{A} + \frac{9\dot{D}}{4H_b^2} \Bigg\{ & 2H_b\ln(X) + \pi X\left[2M(1-M)\sqrt{D} + 2M(M-1)\sqrt{D + \frac{H_b}{M}}\right. \\ & \left. - \frac{MH_b}{D^{1/2}} - \frac{H_b^2}{12D^{3/2}}\right] + \left[H_b(3-M) + (H_b + MD)(1-M)\ln(M) + \frac{H_b^2}{6D}\right]\Bigg\}. \end{aligned} \tag{3.10}$$

Let us now study the outer problem and associated outer solution $\Delta_{out}(X, T)$. For X large enough, (3.6) can be approximated by

$$\Delta_{out}'' - Bo\,\Delta_{out} = -\frac{9\dot{D}}{2H_b X^2}. \tag{3.11}$$

We stress that it is essential here to keep a non-zero right-hand-side source term in the equation, in order to generate a logarithmic contribution as in the inner case. The solution of this equation, satisfying the boundary condition $\Delta_{out} \to 0$ at $X \to \infty$, reads

$$\Delta_{out} = \mathcal{B}\,\mathrm{e}^{-X\sqrt{Bo}} + \frac{9\dot{D}}{4H_b}\left(\exp(-X\sqrt{Bo})\int_{-\infty}^{X\sqrt{Bo}}\frac{\mathrm{e}^t}{t}\,\mathrm{d}t - \exp(X\sqrt{Bo})\int_{X\sqrt{Bo}}^{\infty}\frac{\mathrm{e}^{-t}}{t}\,\mathrm{d}t\right), \tag{3.12}$$

where $\mathcal{B}$ is a function of T only. The small-X behaviour of this inner solution reads

$$\Delta_{out} \sim \mathcal{B}(1 - X\sqrt{Bo}) + \frac{9\dot{D}}{2H_b}\left[\gamma + \frac{1}{2}\ln(Bo) + \ln(X)\right], \tag{3.13}$$

where γ is the Euler constant.

Matching (3.13) and (3.10) allows us to determine the two unknown functions as

$$\mathcal{A} = \mathcal{B} + \frac{9\dot{D}}{4H_b^2}\left[H_b(M-3) + (H_b + MD)(M-1)\ln(M) - \frac{H_b^2}{6D}\right] + \frac{9\dot{D}\gamma}{2H_b} + \frac{9\dot{D}}{4H_b}\ln(Bo), \tag{3.14}$$

$$\mathcal{B} = \frac{9\dot{D}\pi}{4H_b^2\sqrt{Bo}}\left[2M(M-1)\sqrt{D} + 2M(1-M)\sqrt{D + \frac{H_b}{M}} + \frac{MH_b}{\sqrt{D}} + \frac{H_b^2}{12D^{3/2}}\right]. \tag{3.15}$$

In addition, using these matching conditions, the central deformation of the fluid interface can be evaluated from $\Delta_{in}(X = 0, T)$, if $Bo \ll 1$, as

$$\Delta_c = \mathcal{A} + \frac{9\dot{D}}{4H_b^2}\{(1-M)(H_b + MD)\ln(H_b + MD) + [H_b + (M-1)D]M\ln(D)\}. \tag{3.16}$$

Finally, using (3.4), (3.5) and (3.7), as well as the above symmetry (2.18*a*,*b*) and boundary conditions (2.19*a*,*b*), we can solve (2.15) and (2.16) numerically at first order in κ, and hence compute the first-order pressure fields. The derivation of these equations and the method for solving them are summarized in Appendix A. The results are discussed below.

4. Discussion

Hereafter, keeping $Bo \ll 1$, we discuss the zeroth-order and first-order solutions, and investigate the influence of the two key parameters: the viscosity ratio M, and the thickness ratio H_b.

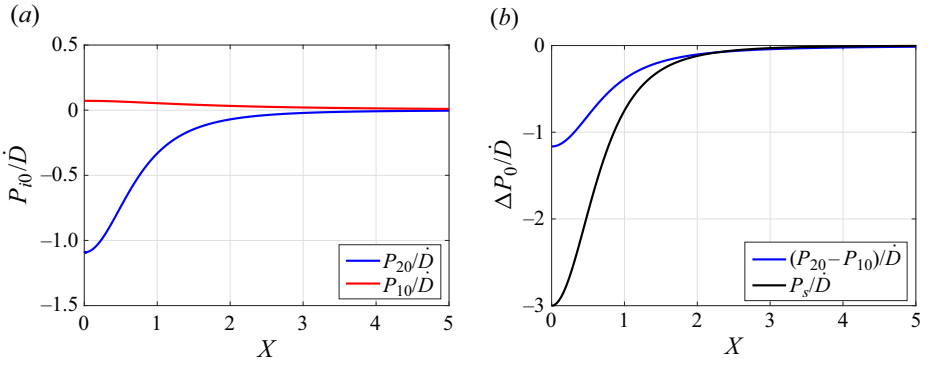

Figure 2. (*a*) Zeroth-order excess pressure fields P_{i0}, normalized by the cylinder's vertical velocity $\dot{D}$, as functions of horizontal coordinate X, as evaluated from (3.4) and (3.5) with $D = 1$, $M = 1.5$ and $H_b = 15$. (*b*) Zeroth-order excess pressure jump $\Delta P_0 = P_{20} - P_{10}$ as a function of horizontal coordinate X, as obtained from (*a*). For comparison, we also show the rigid-case excess pressure $P_s = -3\dot{D}/(D + X^2)^2$ (Jeffrey & Onishi 1981).

4.1. *Zeroth-order pressure*

In figure 2, we plot the zeroth-order excess pressure fields. For comparison, we also show the rigid-case excess pressure $P_s = -3\dot{D}/(D + X^2)^2$ (Jeffrey & Onishi 1981). As we can see, the pressure fields have opposite signs in the two layers. Moreover, the pressure in the top layer is reduced in the case of an undeformable fluid interface, as compared to the no-slip rigid case. This is due to the fact that horizontal motion at the fluid interface is possible in the former case, which reduces the velocity gradients and stresses. Also, we stress that despite their logarithmic forms in (3.4) and (3.5), the zeroth-order pressure fields in both layers decay algebraically towards zero at large X.

Let us now investigate the role of the viscosity ratio M. The results are shown in figure 3. Increasing M, i.e. increasing the viscosity of the bottom liquid layer as compared to the top one, increases the pressure in both layers. This is expected, since increasing the viscosity ratio makes it harder to generate a flow within the bottom layer, which then gets closer to a rigid wall. This is supported by the curves in figure 3(*b*) and by (3.5), where, at high values of M, P_{20} saturates to P_s. An interesting point to note in figure 3(*a*) and (3.4) is that the excess pressure in the bottom layer increases with M as well, but saturates to $9\dot{D}/[2H_b(D + X^2)]$ at large M, which is dependent on the bottom layer thickness H_b. On the other hand, if M is decreased towards zero, then (3.4) predicts that the excess pressure in the bottom layer vanishes completely. Besides, if M is decreased towards zero, then (3.5) predicts that the excess pressure in the top layer saturates to a quarter of the no-slip rigid-wall value, which is the result expected for an effective full-slip interface (i.e. with infinite slip length). The pressure in the top layer is thus bounded at both extremes in M.

The other important parameter to scan and study is the dimensionless bottom-layer thickness H_b. Results are shown in figure 4. Increasing H_b reduces the excess pressure fields in both layers. The two limiting behaviours for P_{20} are the same as when varying M, as expected from (3.4) and (3.5), where it can be seen that the parameter M/H_b is the relevant one.

4.2. *Interface deflection*

The first-order interface deflection is evaluated numerically from (3.7) and plotted in figure 5, along with the matched inner and outer solutions, given by (3.9) and (3.12).

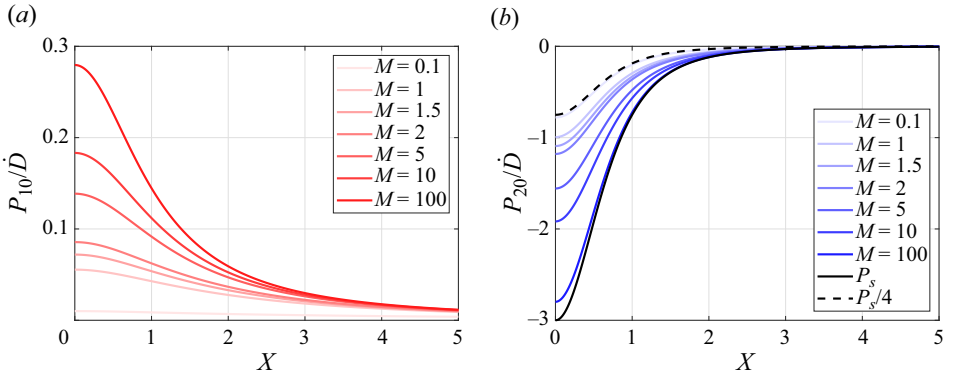

Figure 3. Zeroth-order excess pressure fields (*a*) P_{10} and (*b*) P_{20}, normalized by the cylinder's vertical velocity $\dot{D}$, as functions of horizontal coordinate X, as evaluated from (3.4) and (3.5) with $D = 1$, $H_b = 15$ and various M as indicated in the legends. For comparison, we also show the no-slip rigid-case excess pressure $P_s = -3\dot{D}/(D + X^2)^2$ (Jeffrey & Onishi 1981), and its analogue for a full-slip rigid substrate, i.e. $P_s/4$.

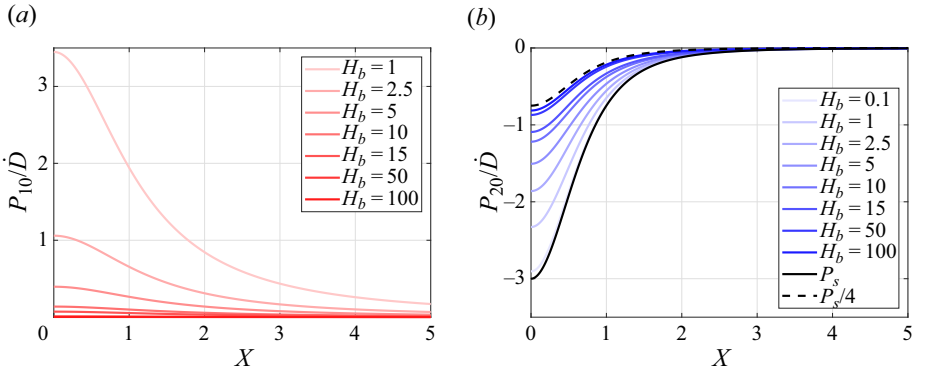

Figure 4. Zeroth-order excess pressure fields (*a*) P_{10} and (*b*) P_{20}, normalized by the cylinder's vertical velocity $\dot{D}$, as functions of horizontal coordinate X, as evaluated from (3.4) and (3.5) with $D = 1$, $M = 1.5$ and various H_b as indicated in the legends. For comparison, we also show the no-slip rigid-case excess pressure $P_s = -3\dot{D}/(D + X^2)^2$ (Jeffrey & Onishi 1981), and its analogue for a full-slip rigid substrate, i.e. $P_s/4$.

It is important to note here that the dimensionless slope is $\epsilon\kappa\Delta'$, and not only Δ'. Therefore, although the values of Δ' may seem large, in the small dimensionless capillary compliance ($\kappa \ll 1$) and lubrication ($\epsilon \ll 1$) limits at stake in our study, the actual slope can still remain small. There is good agreement between the outer and general solutions, except in close proximity to the origin where the outer solution diverges logarithmically. In contrast, while unbounded in the far field, the inner solution agrees well with the general one near the origin.

Let us now investigate the effects of viscosity ratio M and dimensionless bottom-layer thickness H_b on the interface deflection. The results are shown in figure 6. We observe that the interface deflection increases with increasing M or decreasing H_b. As discussed in the previous subsection, for vanishing M or infinite H_b, the zeroth-order top-layer pressure P_{20} reaches $P_s/4$, while the zeroth-order bottom-layer pressure P_{10} vanishes, which leads to the minimal deflection profile. In contrast, as M goes to infinity, P_{20} reaches P_s, while P_{10} increases to a function depending upon H_b. Thus the deflection saturates to

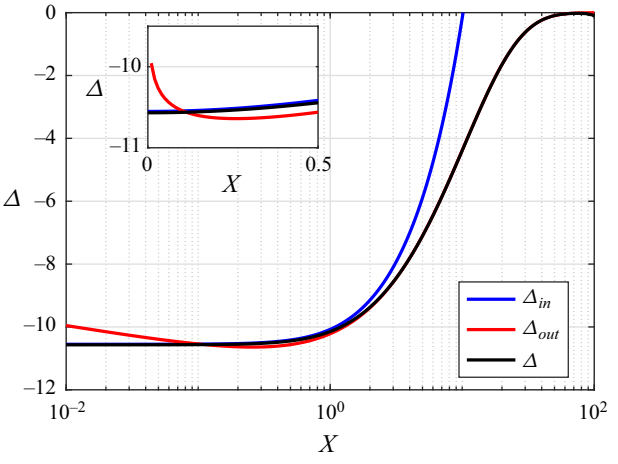

Figure 5. Normalized first-order interface deflection Δ as a function of horizontal coordinate X (black line), as calculated from (3.7), for $M = 1.5$, $H_b = 15$, $Bo = 0.01$, $D = 1$ and $\dot{D} = -1$ (i.e. the cylinder approaching the interface). For comparison, the matched inner (blue) and outer (red) solutions, given by (3.9) and (3.12), respectively, are shown. The inset shows a zoom of the small-X region.

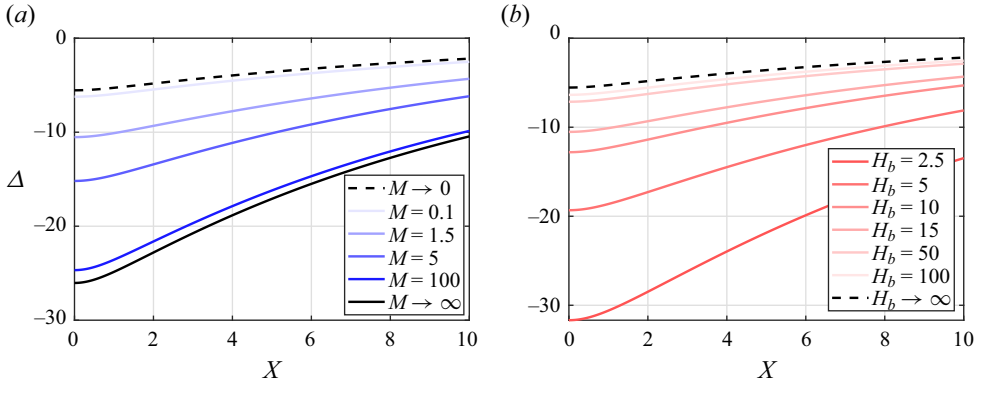

Figure 6. (*a*) Normalized first-order interface deflection Δ as a function of horizontal coordinate X, as calculated from (3.7), for $H_b = 15$, $Bo = 0.01$, $D = 1$, $\dot{D} = -1$ (i.e. the cylinder approaching the interface), and various M as indicated. (*b*) Same as (*a*) for $M = 1.5$ and various H_b as indicated.

an H_b-dependent profile. However, we stress that decreasing H_b increases the deflection without any limit, as the zeroth-order pressure in the bottom layer does not have an upper bound in this case. In reality, such diverging pressure and thus interface deflection would require the consideration of higher-order, nonlinear effects in dimensionless capillary compliance.

4.3. *First-order pressure*

Integrating (2.15) and (2.16) numerically at first order in κ allows us to find the first-order pressure correction. Note that we consider only the first-order top-layer pressure κP_{21}, for two reasons. First, this contribution is the only one required to eventually compute the first-order force exerted on the cylinder (see next subsection). Second, the first-order bottom-layer pressure decays slowly in X, and seems to depend on the size of the numerical

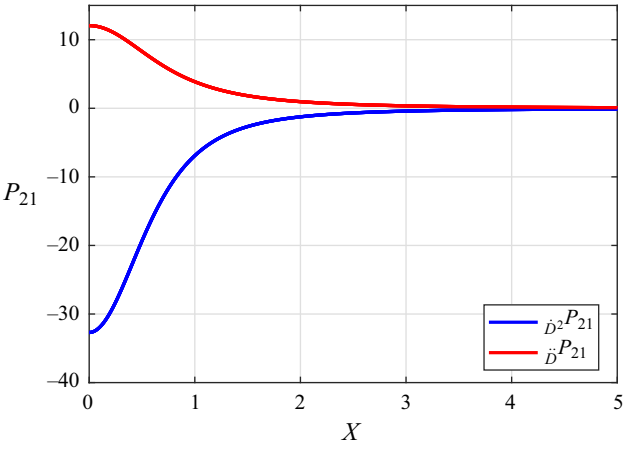

Figure 7. Dynamic adhesive-like (blue) and inertia-like (red) contributions of the first-order pressure correction P_{21} in the top layer as a function of the horizontal coordinate X, obtained from numerical integration of (2.15) and (2.16), for $M = 1.5$, $H_b = 15$, $Bo = 0.01$, $D = 1$, $\dot{D} = -1$ and $\ddot{D} = 1$.

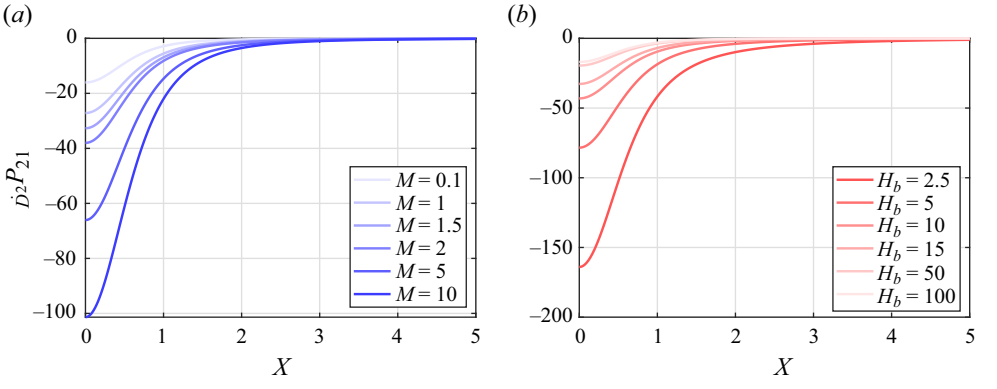

Figure 8. (*a*) Dynamic adhesive-like contribution $\dot{D}^2P_{21}$ of the first-order pressure correction in the top layer as a function of the horizontal coordinate X, obtained from numerical integration of (2.15) and (2.16), for $H_b = 15$, $Bo = 0.01$, $D = 1$, $\dot{D} = -1$, and various M as indicated. (*b*) Same as (*a*) for $M = 1.5$ and various H_b as indicated.

window, indicating the potential need for a far-field regularization. Besides, we decompose P_{21} into two contributions: (i) a dynamic adhesive-like term $\dot{D}^2P_{21}$, depending on the square of the vertical velocity of the cylinder, which tends to attract the moving object towards the deformable interface (Kaveh *et al.* 2014; Salez & Mahadevan 2015; Wang *et al.* 2015; Bertin *et al.* 2022); and (ii) an inertia-like term $\ddot{D}P_{21}$, depending on the vertical acceleration of the cylinder, which is present here as a consequence of volume conservation (Salez & Mahadevan 2015; Bertin *et al.* 2022), even though the governing equations are free of inertia. The results are shown in figures 7, 8 and 9. We see that both pressure contributions are maximal at the centre ($X = 0$) and vanish quickly above $X \sim 1$. Besides, changing the viscosity ratio M and the dimensionless bottom-layer thickness H_b have the same effects as for the zeroth-order case.

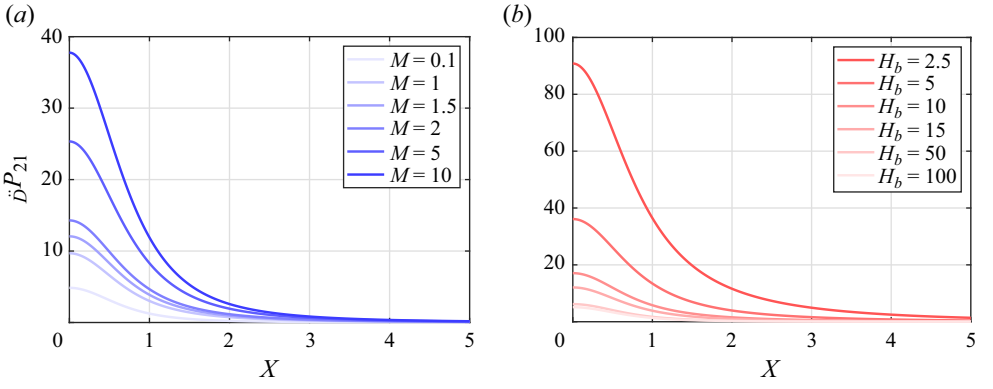

Figure 9. (*a*) Inertia-like contribution $_{\ddot{D}}P_{21}$ of the first-order pressure correction in the top layer as a function of the horizontal coordinate X, obtained from numerical integration of (2.15) and (2.16), for $H_b = 15$, $Bo = 0.01$, $D = 1$, $\dot{D} = -1$, $\ddot{D} = 1$, and various M as indicated. (*b*) Same as (*a*) for $M = 1.5$ and various H_b as indicated.

4.4. *Capillary-lubrication force*

Since viscous stresses are negligible as compared to the excess pressure field within the lubrication framework, and since typically the excess pressure field obtained above vanishes beyond $X \sim 1$ in the top layer, the normal capillary-lubrication force per unit length felt by the cylinder can be evaluated simply by integrating the excess pressure field in the top layer along the horizontal coordinate. Putting back dimensions, the force per unit length thus reads at first order in capillary compliance:

$$\begin{aligned} F = \int_{-\infty}^{+\infty} \mathrm{d}x\, p_2 \simeq & -\eta_2 \dot{d} \left(\frac{a}{d}\right)^{3/2} \phi_0 \left(\frac{MD}{H_b}\right) \\ & - \frac{\eta_2^2 \dot{d}^2}{\sigma} \left(\frac{a}{d}\right)^{7/2} {}_{\dot{D}^2}\phi_1(M, H_b, Bo, D) \\ & + \frac{\eta_2^2 \ddot{d} a}{\sigma} \left(\frac{a}{d}\right)^{5/2} {}_{\ddot{D}}\phi_1(M, H_b, Bo, D), \end{aligned} \tag{4.1}$$

where ϕ_0, $_{\dot{D}^2}\phi_1$ and $_{\ddot{D}}\phi_1$ are auxiliary functions depending on the parameters of the problem, M, H_b, as well as Bo, and importantly, potentially having extra dependencies in d through D.

Let us first study the zeroth-order contribution to the force, through the auxiliary function ϕ_0. By integrating (3.5), one can calculate ϕ_0 and show that it depends only on the variable MD/H_b. The function is shown in figure 10. It is always positive, indicating a Stokes-like drag effect. At infinite MD/H_b, one recovers the no-slip rigid case (Jeffrey & Onishi 1981), and the scaling of the force with d is thus $\sim d^{-3/2}$. At vanishing MD/H_b, ϕ_0 saturates to a quarter of the no-slip rigid value, which corresponds to the case of a full-slip rigid wall, with pressure $P_s/4$ as discussed above, and the scaling is once again $\sim d^{-3/2}$. In between these limits, we observe a smooth crossover and there is thus no clear power law in d.

Then we study the first-order contributions to the force, through the two auxiliary functions $_{\dot{D}^2}\phi_1$ and $_{\ddot{D}}\phi_1$. In these cases, there does not seem to be a simple combination of the parameters M, H_b, Bo and variable D that controls the auxiliary functions. These are evaluated numerically by integration of P_{21}, and plotted in figure 11 for various parameters. The two auxiliary functions are always positive and grow with increasing M

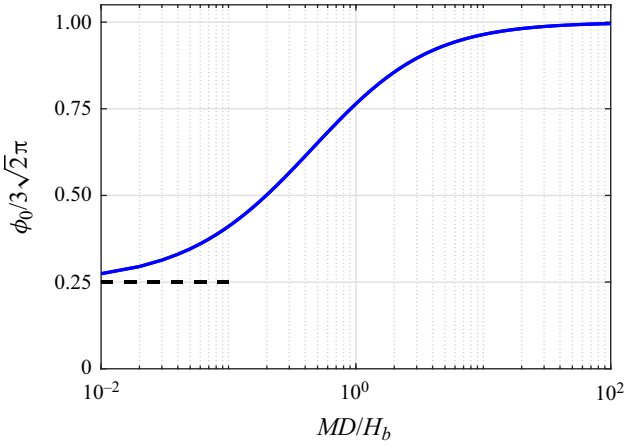

Figure 10. Zeroth-order auxiliary function ϕ_0 of the normal force (see (4.1)) obtained by integrating (3.5), and normalized by the corresponding value $3\sqrt{2}\pi$ of the no-slip rigid case (Jeffrey & Onishi 1981), as a function of the single rescaled variable MD/H_b. The dashed line shows a constant value $1/4$.

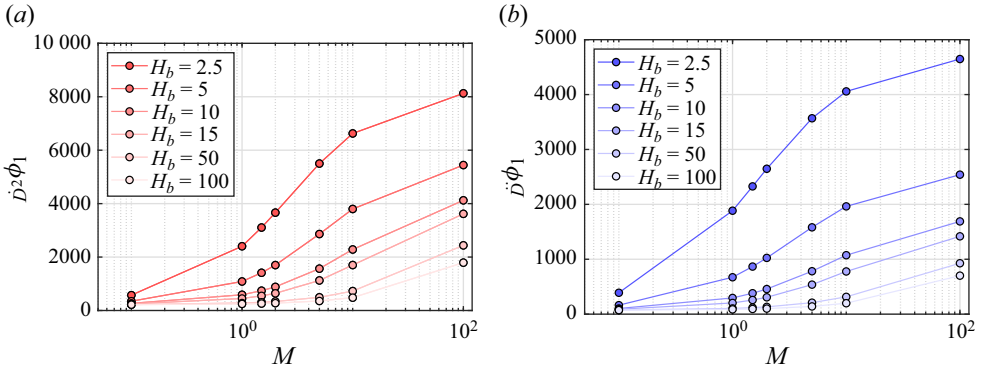

Figure 11. First-order auxiliary functions (*a*) $_{\dot{D}^2}\phi_1$ and (*b*) $_{\ddot{D}}\phi_1$ of the normal force (see (4.1)), as functions of the viscosity ratio M, as obtained from numerical integration of the first-order excess pressure P_{21} in the top layer, for $Bo = 0.01$, $D = 1$, and various values of the dimensionless bottom-layer thickness H_b, as indicated. The lines are guides for the eye.

or decreasing H_b. They seem to saturate at either vanishing M or infinite H_b. At infinite M, there might be a saturation as well. However, the functions seem unbounded when decreasing H_b. As a remark, the important increase observed for the auxiliary functions in some parametric ranges enforces stringent conditions on the dimensionless capillary compliance κ so as to be in line with the perturbative approach.

Finally, we wish to discuss briefly the corresponding three-dimensional problem of a sphere approaching the interface. In such a case, not only does the calculation procedure of the force and the deflection remain analogous to the current problem, but the dimensionless capillary compliance κ remains unchanged from the two-dimensional case, as the scales of the lubrication pressure and the Laplace pressure jump remain the same. Apart from modified numerical prefactors, the essential modification emerges in the scale of the forces, through a multiplication of the two-dimensional force per unit length by the relevant length scale in the third direction of space. This new length scale is the hydrodynamic

radius, which implies that the zeroth-order force scales as $\sim\eta_2\dot{d}a^2/d$, and that the two components of the first-order force scale as $\sim\eta_2^2\dot{d}^2a^4/(\sigma d^3)$ and $\sim\eta_2^2\ddot{d}a^4/(\sigma d^2)$.

5. Conclusion

We have studied theoretically and numerically the capillary-lubrication force felt by an immersed infinite cylinder when approaching a thin viscous film supported on a rigid substrate. While the analogous scenario near an elastic wall has been studied extensively in recent years, our work investigated the influence of a fluid interface on such an emerging force by employing similar tools and a perturbation analysis in capillary compliance. In particular, we investigated the roles of two key dimensionless parameters: the viscosity ratio and the thickness ratio between the two layers.

As opposed to the case of a rigid wall, the zeroth-order (i.e. with no vertical deformation of the interface) pressure fields in both layers appeared to become logarithmic in space rather than rational functions, except in the far field, where asymptotic algebraic decays were recovered. Also, increasing the viscosity of the bottom layer, or reducing its thickness, led to a saturation towards the no-slip rigid-like behaviour. In contrast, a full-slip rigid behaviour was observed with the reduction of the bottom-layer viscosity, or the increase of the bottom-layer thickness. These zeroth-order pressure fields generate a long-range deflection of the interface, which was computed numerically along with an asymptotic study at small Bond numbers. Limiting behaviours of the interface deflection were observed with increasing or decreasing viscosity of the bottom layer, as well as increasing thickness. However, no limit was observed with the reduction of the bottom-layer thickness, and one thus expects nonlinearities to eventually regularize such a behaviour.

The first-order perturbations to the pressure fields due to the deformed interface were finally computed numerically, hence providing the correction to the Stokes drag felt by a particle due to the nearby deformable fluid interface. We identified two main dynamic contributions – (i) a velocity-dependent adhesive-like one, and (ii) an acceleration-dependent inertia-like one – and we used them to compute the total dimensionless force felt by the cylinder as it approaches the interface. The adhesive-like contribution essentially reduces the drag, while the inertia-like contribution increases it. The auxiliary functions that calculate the influence of viscosity and thickness ratios on the force were also evaluated and were seen to show limiting behaviours with increasing or decreasing bottom-layer viscosity and increasing bottom-layer thickness. Our results might find applications in confined colloidal and biophysical systems.

Funding. The authors thank V. Bertin, A. Carlson and C. Pedersen for interesting discussions. They acknowledge financial support from the European Union through the European Research Council under an EMetBrown (ERC-CoG-101039103) grant. Views and opinions expressed are, however, those of the authors only, and do not necessarily reflect those of the European Union or the European Research Council. Neither the European Union nor the granting authority can be held responsible for them. The authors also acknowledge financial support from the Agence Nationale de la Recherche under EMetBrown (ANR-21-ERCC-0010-01), Softer (ANR-21-CE06-0029) and Fricolas (ANR-21-CE06-0039) grants. Finally, they thank the Soft Matter Collaborative Research Unit, Frontier Research Center for Advanced Material and Life Science, Faculty of Advanced Life Science at Hokkaido University, Sapporo, Japan.

Declaration of interests. The authors report no conflict of interest.

Author ORCIDs.
Thomas Salez https://orcid.org/0000-0001-6111-8721.

Appendix A. First-order equations

The dimensionless fluxes in both layers can be written as

$$Q_1 = F_1(H_1, H_2)\, P_1' + F_2(H_1, H_2)\, P_2', \tag{A1}$$

$$Q_2 = F_3(H_1, H_2)\, P_1' + F_4(H_1, H_2)\, P_2', \tag{A2}$$

where the F_i are the auxiliary functions found in (2.13) and (2.14), which depend on H_1 and H_2. While $H_2 = D(T) + X^2$ is a function that is independent of the interface deflection, H_1 depends on the interface deflection and thus changes with the order of the equation. Taylor expansions of the auxiliary functions at first order in κ give us

$$F_i(H_1, H_2) \simeq F_i(H_b, H_2) + \kappa\Delta \left.\frac{\partial F_i}{\partial H_1}\right|_{H_1=H_b} + O(\kappa^2). \tag{A3}$$

Since the auxiliary functions are known functions of H_1, we can calculate easily their partial derivatives with respect to H_1, which are denoted by $G_i = \partial F_i/\partial H_1$. Hence the fluxes above can be approximated at first order in compliance, as

$$\begin{aligned} Q_1 \simeq\ & [F_1(H_b, H_2)\, P_{10}' + \kappa(F_1(H_b, H_2)\, P_{11}' + \Delta G_1(H_b, H_2)\, P_{10}')] \\ & + [F_2(H_b, H_2)\, P_{20}' + \kappa(F_2(H_b, H_2)\, P_{21}' + \Delta G_2(H_b, H_2)\, P_{20}')] + O(\kappa^2), \end{aligned} \tag{A4}$$

$$\begin{aligned} Q_2 \simeq\ & [F_3(H_b, H_2)\, P_{10}' + \kappa(F_3(H_b, H_2)\, P_{11}' + \Delta G_3(H_b, H_2)\, P_{10}')] \\ & + [F_4(H_b, H_2)\, P_{20}' + \kappa(F_4(H_b, H_2)\, P_{21}' + \Delta G_4(H_b, H_2)\, P_{20}')] + O(\kappa^2). \end{aligned} \tag{A5}$$

The κ-independent parts of these equations correspond to the fluxes at zeroth order, and can be used in conjunction with (2.15) and (2.16) in order to obtain the analytical expressions of the zeroth-order pressure fields (see (3.4) and (3.5)). Furthermore, the above fluxes can be combined in order to derive the thin-film equations at $O(\kappa)$, which read

$$\begin{aligned} \frac{\partial\Delta}{\partial T} = & -\frac{\partial}{\partial X}[F_1(H_b, H_2)\, P_{11}' + \Delta G_1(H_b, H_2)\, P_{10}' + F_2(H_b, H_2)\, P_{21}' \\ & + \Delta G_2(H_b, H_2)\, P_{20}'], \end{aligned} \tag{A6}$$

$$\frac{\partial\Delta}{\partial T} = \frac{\partial}{\partial X}[F_3(H_b, H_2)\, P_{11}' + \Delta G_3(H_b, H_2)\, P_{10}' + F_4(H_b, H_2)\, P_{21}' + \Delta G_4(H_b, H_2)\, P_{20}']. \tag{A7}$$

These equations can be spatially integrated once, and rearranged to give

$$F_1(H_b, H_2)\, P_{11}' + F_2(H_b, H_2)\, P_{21}' = -\int_0^X \frac{\partial\Delta}{\partial T}\,\mathrm{d}X - \mathcal{J}_1, \tag{A8}$$

$$F_3(H_b, H_2)\, P_{11}' + F_4(H_b, H_2)\, P_{21}' = \int_0^X \frac{\partial\Delta}{\partial T}\,\mathrm{d}X - \mathcal{J}_2, \tag{A9}$$

where we have invoked two new auxiliary functions:

$$\mathcal{J}_1 = \Delta G_1(H_b, H_2)\, P_{10}' + \Delta G_2(H_b, H_2)\, P_{20}', \tag{A10}$$

$$\mathcal{J}_2 = \Delta G_3(H_b, H_2)\, P_{10}' + \Delta G_4(H_b, H_2)\, P_{20}'. \tag{A11}$$

Then the derivatives of the first-order pressure fields read

$$P'_{11} = \frac{F_4\mathcal{H}_1 - F_2\mathcal{H}_2}{F_4F_1 - F_2F_3}, \tag{A12}$$

$$P'_{21} = -\frac{F_3\mathcal{H}_1 - F_1\mathcal{H}_2}{F_4F_1 - F_2F_3}, \tag{A13}$$

where $\mathcal{H}_1$ and $\mathcal{H}_2$ denote the right-hand sides of (A8) and (A9). The above expressions can be integrated over X, imposing the vanishing of the pressure in the far field, to give us the first-order pressure fields. We note that the above equations are linear combinations of $\mathcal{H}_1$ and $\mathcal{H}_2$. This property is exploited directly in order to calculate separately the components of the first-order pressure fields depending on the acceleration and the squared velocity. To this aim, we introduce two new auxiliary functions:

$$\mathcal{Q}_1 = \int_0^X \left.\frac{\partial\Delta}{\partial T}\right|_{\dot{D}^2} \mathrm{d}X, \tag{A14}$$

$$\mathcal{Q}_2 = \int_0^X \left.\frac{\partial\Delta}{\partial T}\right|_{\ddot{D}} \mathrm{d}X, \tag{A15}$$

that denote the integrals of the time derivatives of the deflection corresponding to the squared-velocity-dependant and acceleration-dependant components, respectively. These time derivatives are found by differentiating the pressure fields with respect to time, as

$$\frac{\partial P_{10}}{\partial T} = \frac{9M\ddot{D}}{2H_b^2}\ln\left(1+\frac{1}{\xi}\right) - \frac{9M^2\dot{D}^2}{2H_b^3}\frac{1}{\xi(\xi+1)}, \tag{A16}$$

$$\frac{\partial P_{20}}{\partial T} = \frac{9M^2\ddot{D}}{2H_b^2}\left[\ln\left(1+\frac{1}{\xi}\right) - \frac{1}{\xi} - \frac{1}{6\xi^2}\right] + \frac{9M^3\dot{D}^2}{2H_b^3}\left[\frac{-1}{\xi(\xi+1)} + \frac{1}{\xi^2} + \frac{1}{3\xi^3}\right], \tag{A17}$$

and injecting the latter expressions inside the integral of (3.7). In the above expressions, we see that the first terms in the right-hand sides characterize the effects of acceleration of the cylinder, while the second terms characterize the effects of squared velocity. Then $\mathcal{Q}_1$ and $\mathcal{Q}_2$ can be evaluated numerically. As opposed to $\mathcal{Q}_1$ and $\mathcal{Q}_2$, both $\mathcal{J}_1$ and $\mathcal{J}_2$ are independent of $\ddot{D}$ but are directly proportional to $\dot{D}^2$, since the deflection Δ and zeroth-order pressure gradients P'_{10} and P'_{20} are proportional to $\dot{D}$. Using the above properties and expressions, we split $\mathcal{H}_1$ and $\mathcal{H}_2$ into acceleration-dependent and squared-velocity-dependent terms as

$$(\mathcal{H}_1)_{\dot{D}^2} = -\mathcal{Q}_1 - \mathcal{J}_1, \tag{A18}$$

$$(\mathcal{H}_2)_{\dot{D}^2} = \mathcal{Q}_1 - \mathcal{J}_2, \tag{A19}$$

$$(\mathcal{H}_1)_{\ddot{D}} = -\mathcal{Q}_2, \tag{A20}$$

$$(\mathcal{H}_2)_{\ddot{D}} = \mathcal{Q}_2, \tag{A21}$$

which are eventually used in (A12) and (A13) in order to calculate the corresponding contributions to the first-order pressure fields separately.

References

Andreotti, B., Baumchen, O., Boulogne, F., Daniels, K.E., Dufresne, E.R., Perrin, H., Salez, T., Snoeijer, J.H. & Style, R.W. 2016 Solid capillarity: when and how does surface tension deform soft solids? *Soft Matt.* **12**, 2993–2996.

Balmforth, N.J., Cawthorn, C.J. & Craster, R.V. 2010 Contact in a viscous fluid. Part 2. A compressible fluid and an elastic solid. *J. Fluid Mech.* **646**, 339.

Basoli, F., Giannitelli, S.M., Gori, M., Mozetic, P., Bonfanti, A., Trombetta, M. & Rainer, A. 2018 Biomechanical characterization at the cell scale: present and prospects. *Front. Physiol.* **9**, 1449.

Batchelor, G.K. 1967 *An Introduction to Fluid Dynamics*. Cambridge University Press.

Beaucourt, J., Biben, T. & Misbah, C. 2004 Optimal lift force on vesicles near a compressible substrate. *Europhys. Lett.* **67**, 676.

Berdan II, C. & Leal, L.G. 1982 Motion of a sphere in the presence of a deformable interface: I. Perturbation of the interface from flat: the effects on drag and torque. *J. Colloid Interface Sci.* **87** (1), 62–80.

Bertin, V., Amarouchene, Y., Raphael, E. & Salez, T. 2022 Soft-lubrication interactions between a rigid sphere and an elastic wall. *J. Fluid Mech.* **933**, A23.

Bertin, V., Zhang, Z., Boisgard, R., Grauby-Heywang, C., Raphaël, E., Salez, T. & Maali, A. 2021 Contactless rheology of finite-size air–water interfaces. *Phys. Rev. Res.* **3** (3), L032007.

Bouchet, A.-S., Cazeneuve, C., Baghdadli, N., Luengo, G.S. & Drummond, C. 2015 Experimental study and modeling of boundary lubricant polyelectrolyte films. *Macromolecules* **48**, 2244.

Bureau, L., Coupier, G. & Salez, T. 2023 Lift a low Reynolds number. arXiv:2207.04538.

Chan, D.Y.C., Klaseboer, E. & Manica, R. 2011 Film drainage and coalescence between deformable drops and bubbles. *Soft Matt.* **7** (6), 2235–2264.

Cooley, M.D.A. & O'Neill, M.E. 1969 On the slow motion generated in a viscous fluid by the approach of a sphere to a plane wall or stationary sphere. *Mathematika* **16** (1), 37–49.

Davies, H.S., Debarre, D., El Amri, N., Verdier, C., Richter, R.P. & Bureau, L. 2018 Elastohydrodynamic lift at a soft wall. *Phys. Rev. Lett.* **120**, 198001.

Dupré de Baubigny, J., Benzaquen, M., Fabié, L., Delmas, M., Aimé, J.-P., Legros, M. & Ondarçuhu, T. 2015 Shape and effective spring constant of liquid interfaces probed at the nanometer scale: finite size effects. *Langmuir* **31** (36), 9790–9798.

Essink, M.H., Pandey, A., Karpitschka, S., Venner, C.H. & Snoeijer, J.H. 2021 Regimes of soft lubrication. *J. Fluid Mech.* **915**.

Garcia, L., Barraud, C., Picard, C., Giraud, J., Charlaix, E. & Cross, B. 2016 A micro-nano-rheometer for the mechanics of soft matter at interfaces. *Rev. Sci. Instrum.* **87** (11), 113906.

Geller, A.S., Lee, S.H. & Leal, L.G. 1986 The creeping motion of a spherical particle normal to a deformable interface. *J. Fluid Mech.* **169**, 27–69.

Goldman, A.J., Cox, R.G. & Brenner, H. 1967 Slow viscous motion of a sphere parallel to a plane wall – I. Motion through a quiescent fluid. *Chem. Engng Sci.* **22** (4), 637–651.

Guan, D., Barraud, C., Charlaix, E. & Tong, P. 2017 Noncontact viscoelastic measurement of polymer thin films in a liquid medium using long-needle atomic force microscopy. *Langmuir* **33** (6), 1385–1390.

Happel, J. & Brenner, H. 1983 *Low Reynolds Number Hydrodynamics: With Special Applications to Particulate Media*, vol. 1. Springer Science & Business Media.

Hocking, L.M. 1973 The effect of slip on the motion of a sphere close to a wall and of two adjacent spheres. *J. Engng Maths* **7** (3), 207–221.

James, D.F. 1974 The meniscus on the outside of a small circular cylinder. *J. Fluid Mech.* **63** (4), 657–664.

Jeffrey, D.J. & Onishi, Y. 1981 The slow motion of a cylinder next to a plane wall. *Q. J. Mech. Appl. Maths* **34** (2), 129–137.

Johnson, K.L. 1985 *Contact Mechanics*. Cambridge University Press.

Karan, P., Chakraborty, J. & Chakraborty, S. 2018 Small-scale flow with deformable boundaries. *J. Indian Inst. Sci.* **98**, 159.

Karan, P., Chakraborty, J. & Chakraborty, S. 2020 Influence of non-hydrodynamic forces on the elastic response of an ultra-thin soft coating under fluid-mediated dynamic loading. *Phys. Fluids* **32** (2).

Karan, P., Chakraborty, J. & Chakraborty, S. 2021 Generalization of elastohydrodynamic interactions between a rigid sphere and a nearby soft wall. *J. Fluid Mech.* **923**, A32.

Kargar-Estahbanati, A. & Rallabandi, B. 2021 Lift forces on three-dimensional elastic and viscoelastic lubricated contacts. *Phys. Rev. Fluids* **6**, 034003.

Kaveh, F., Ally, J., Kappl, M. & Butt, H.-J. 2014 Hydrodynamic force between a sphere and a soft, elastic surface. *Langmuir* **30** (39), 11619–11624.

Kopecz-Muller, C., Bertin, V., Raphaël, E., McGraw, J.D. & Salez, T. 2023 Mechanical response of a thick poroelastic gel in contactless colloidal-probe rheology. *Proc. R. Soc.* A **479**, 20220832.

Leal, L.G. 2007 *Advanced Transport Phenomena: Fluid Mechanics and Convective Transport Processes*, vol. 7. Cambridge University Press.

LEE, S.H., CHADWICK, R.S. & LEAL, L.G. 1979 Motion of a sphere in the presence of a plane interface. Part 1. An approximate solution by generalization of the method of Lorentz. *J. Fluid Mech.* **93** (4), 705–726.

LEE, S.H. & LEAL, L.G. 1980 Motion of a sphere in the presence of a plane interface. Part 2. An exact solution in bipolar co-ordinates. *J. Fluid Mech.* **98** (1), 193–224.

LEE, S.H. & LEAL, L.G. 1982 The motion of a sphere in the presence of a deformable interface: II. A numerical study of the translation of a sphere normal to an interface. *J. Colloid Interface Sci.* **87** (1), 81–106.

LEROY, S. & CHARLAIX, E. 2011 Hydrodynamic interactions for the measurement of thin film elastic properties. *J. Fluid Mech.* **674**, 389–407.

LEROY, S., STEINBERGER, A., COTTIN-BIZONNE, C., RESTAGNO, F., LÉGER, L. & CHARLAIX, E. 2012 Hydrodynamic interaction between a spherical particle and an elastic surface: a gentle probe for soft thin films. *Phys. Rev. Lett.* **108** (26), 264501.

LI, J. & CHOU, T.-W. 1997 Elastic field of a thin-film/substrate system under an axisymmetric loading. *Intl J. Solids Struct.* **34** (35–36), 4463–4478.

LO, L.L. 1983 The meniscus on a needle – a lesson in matching. *J. Fluid Mech.* **132**, 65–78.

LOPEZ, D. & LAUGA, E. 2014 Dynamics of swimming bacteria at complex interfaces. *Phys. Fluids* **26** (7), 400–412.

MAALI, A., BOISGARD, R., CHRAIBI, H., ZHANG, Z., KELLAY, H. & WÜRGER, A. 2017 Viscoelastic drag forces and crossover from no-slip to slip boundary conditions for flow near air–water interfaces. *Phys. Rev. Lett.* **118**, 084501.

NOGI, T. & KATO, T. 1997 Influence of a hard surface layer on the limit of elastic contact. Part 1. Analysis using a real surface model. *J. Tribol.* **119** (3), 493–500.

NOGI, T. & KATO, T. 2002 Influence of a hard surface layer on the limit of elastic contact. Part 2. Analysis using a modified GW model. *J. Trib.* **124** (4), 785–793.

O'NEILL, M.E. & STEWARTSON, K. 1967 On the slow motion of a sphere parallel to a nearby plane wall. *J. Fluid Mech.* **27** (4), 705–724.

ORON, A., DAVIS, S. & BANKOFF, S. 1997 Long-scale evolution of thin liquid films. *Rev. Mod. Phys.* **69**, 931.

PANDEY, A., KARPITSCHKA, S., VENNER, C.H. & SNOEIJER, J.H. 2016 Lubrication of soft viscoelastic solids. *J. Fluid Mech.* **799**, 433–447.

RALLABANDI, B., OPPENHEIMER, N., ZION, M.Y.B. & STONE, H.A. 2018 Membrane-induced hydroelastic migration of a particle surfing its own wave. *Nat. Phys.* **14**, 1211.

REYNOLDS, O. 1886 On the theory of lubrication and its application to Mr Beauchamp Tower's experiments, including an experimental determination of the viscosity of olive oil. *Phil. Trans. R. Soc. Lond.* **177**, 157.

RINEHART, A., LACIS, U., SALEZ, T. & BAGHERI, S. 2020 Lift induced by slip inhomogeneities in lubricated contacts. *Phys. Rev. Fluids* **5**, 082001.

SAINTYVES, B., JULES, T., SALEZ, T. & MAHADEVAN, L. 2016 Self-sustained lift and low friction via soft lubrication. *Proc. Natl Acad. Sci. USA* **113** (21), 5847–5849.

SALEZ, T. & MAHADEVAN, L. 2015 Elastohydrodynamics of a sliding, spinning and sedimenting cylinder near a soft wall. *J. Fluid Mech.* **779**, 181–196.

SEKIMOTO, K. & LEIBLER, L. 1993 A mechanism for shear thickening of polymer-bearing surfaces: elasto-hydrodynamic coupling. *Europhys. Lett.* **23** (2), 113.

SKOTHEIM, J.M. & MAHADEVAN, L. 2005 Soft lubrication: the elastohydrodynamics of nonconforming and conforming contacts. *Phys. Fluids* **17** (9), 092101.

SNOEIJER, J.H., EGGERS, J. & VENNER, C.H. 2013 Similarity theory of lubricated Hertzian contacts. *Phys. Fluids* **25** (10), 101705.

TROUILLOUD, R., TONY, S.Y., HOSOI, A.E. & LAUGA, E. 2008 Soft swimming: exploiting deformable interfaces for low Reynolds number locomotion. *Phys. Rev. Lett.* **101** (4), 048102.

URZAY, J., LLEWELLYN SMITH, S.G. & GLOVER, B.J. 2007 The elastohydrodynamic force on a sphere near a soft wall. *Phys. Fluids* **19** (10), 103106.

VAKARELSKI, I.U., MANICA, R., TANG, X., O'SHEA, S.J., STEVENS, G.W., GRIESER, F., DAGASTINE, R.R. & CHAN, D.Y.C. 2010 Dynamic interactions between microbubbles in water. *Proc. Natl Acad. Sci. USA* **107** (25), 11177–11182.

VIALAR, P., MERZEAU, P., GIASSON, S. & DRUMMOND, C. 2019 Compliant surfaces under shear: elastohydrodynamic lift force. *Langmuir* **35** (48), 15605–15613.

VILLEY, R., MARTINOT, E., COTTIN-BIZONNE, C., PHANER-GOUTORBE, M., LÉGER, L., RESTAGNO, F. & CHARLAIX, E. 2013 Effect of surface elasticity on the rheology of nanometric liquids. *Phys. Rev. Lett.* **111**, 215701.

WANG, Y., DHONG, C. & FRECHETTE, J. 2015 Out-of-contact elastohydrodynamic deformation due to lubrication forces. *Phys. Rev. Lett.* **115** (24), 248302.

WEEKLEY, S.J., WATERS, S.L. & JENSEN, O.E. 2006 Transient elastohydrodynamic drag on a particle moving near a deformable wall. *Q. J. Mech. Appl. Maths* **59** (2), 277.

YANG, S.-M. & LEAL, L.G. 1983 Particle motion in Stokes flow near a plane fluid–fluid interface. Part 1. Slender body in a quiescent fluid. *J. Fluid Mech.* **136**, 393–421.

ZHANG, Z., ARSHAD, M., BERTIN, V., ALMOHAMAD, S., RAPHAËL, E., SALEZ, T. & MAALI, A. 2022 Contactless rheology of soft gels over a broad frequency range. *Phys. Rev. Appl.* **17** (6), 064045.

ZHANG, Z., BERTIN, V., ARSHAD, M., RAPHAEL, E., SALEZ, T. & MAALI, A. 2020 Direct measurement of the elastohydrodynamic lift force at the nanoscale. *Phys. Rev. Lett.* **124** (5), 054502.